Available online at www.sciencedirect.com
SCIENCE DIRECT®
International Journal of Heat and Mass Transfer 49 (2006) 4340–4351
International Journal of HEAT and MASS TRANSFER
www.elsevier.com/locate/ijhmt

Simulation of turbulent natural convection in a porous cylindrical annulus using a macroscopic two-equation model

Edimilson J. Braga, Marcelo J.S. de Lemos *

Departamento de Energia – IEME, Instituto Tecnológico de Aeronáutica – ITA, 12228-900 São José dos Campos, SP, Brazil

Received 19 October 2004; received in revised form 7 April 2006
Available online 25 July 2006

Abstract

This work presents numerical computations for laminar and turbulent natural convection within a horizontal cylindrical annulus filled with a fluid saturated porous medium. Computations covered the range $25 < Ra_m < 500$ and $3.2 \times 10^{-4} > Da > 3.2 \times 10^{-6}$ and made use of the finite volume method. The inner and outer walls are maintained at constant but different temperatures. The macroscopic k–ε turbulence model with wall function is used to handle turbulent flows in porous media. First, the turbulence model is switched off and the laminar branch of the solution is found when increasing the Rayleigh number, Ra_m. Subsequently, the turbulence model is included and calculations start at high Ra_m, merging to the laminar branch for a reducing Ra_m. This convergence of results as Ra_m decreases can be seen as an estimate of the so-called laminarization phenomenon. Here, a critical Rayleigh number was not identified and results indicated that when the porosity, Prandtl number, conductivity ratio between the fluid and the solid matrix and Ra_m are kept fixed, the lower the Darcy number, the higher is the difference of the average Nusselt number given by the laminar and turbulent models.

Keywords: Turbulence modeling; Porous media; Natural convection; Cylindrical annuli

1. Introduction

The analyses of natural convection in a horizontal cylindrical annuli filled by a porous material has been subject of a number of studies in recent years. Thermal insulators, cryogenics, thermal storage systems, electronic cooling, inert gas insulation of high-voltage electric cables and the determination of the requirements for aircraft cabin insulation are some examples of applications.

The first basic study on natural convection in clear cylindrical annuli was carried out by [1] and extended by [2]. A very extensive analysis has been made on the concentric annuli by [3]. They have conducted both numerical simulation using the finite elements technique and experimental studies using Mach-Zehnder interferometer. Application of other type of finite differences method with ADI numerical solution has also reported by [4] in solving the laminar horizontal concentric annuli problem formulated in cylindrical polar coordinates. Small eccentric annuli has performed in the work of [5], using an expansion in terms of the double series of eccentricity and Rayleigh number for small values of Ra. The work of [6] extended the knowledge on the natural convection heat transfer in the horizontal cylindrical annuli and the numerical analysis has been made using finite difference method in a bipolar coordinate system based on successive over-relaxation iteration.

Flow analysis on clear concentric annulus has been extended to turbulent natural convection using a two-equation turbulence model in the work of [7]. Experimental works yielded new information about the field variable, primarily on the distribution of the mean temperature in the fluid and of Nusselt number around the cylinders circumference in the work of [8]. The turbulence appears in the upper region of the annulus in the plume above the heated inner cylinder. On the other hand, the stable stratification below

* Corresponding author. Tel.: +55 12 3947 5860; fax: +55 12 3947 5842.
E-mail address: delemos@mec.ita.br (M.J.S. de Lemos).

0017-9310/$ - see front matter © 2006 Elsevier Ltd. All rights reserved.
doi:10.1016/j.ijheatmasstransfer.2006.04.032

Nomenclature

c_F	Forchheimer coefficient
c's	non-dimensional turbulence model constants
c_p	specific heat
d	pore diameter
$\mathbf{D}$	$\mathbf{D} = [\nabla\mathbf{u} + (\nabla\mathbf{u})^T]/2$, deformation rate tensor
Da	Darcy number, $Da = \frac{K}{r_i^2}$
D_p	particle diameter
$\mathbf{g}$	gravity acceleration vector
G^i	generation rate of $\langle k\rangle^i$ due to the action of the porous matrix
G^i_β	generation rate of $\langle k\rangle^i$ due to the buoyant effects
h	heat transfer coefficient
$\mathbf{I}$	unit tensor
K	$K = \frac{D_p^2\phi^3}{144(1-\phi)^2}$, permeability
k	$k = \overline{\mathbf{u}'\cdot\mathbf{u}'}/2$, turbulent kinetic energy per mass unit
k_f	fluid thermal conductivity
k_s	solid thermal conductivity
$\mathbf{K}_{disp}$	conductivity tensor due to the dispersion
$\mathbf{K}_{disp,t}$	conductivity tensor due to the turbulent dispersion
$\mathbf{K}_t$	conductivity tensor due to the turbulent heat flux
$\mathbf{K}_{tor}$	conductivity tensor due to the tortuosity
Nu	Nusselt number
Pe	Peclet number
Pe_D	modified Peclet number, $Pe_D = Pe(1-\phi)^{1/2}$
P^i	production rate of $\langle k\rangle^i$ due to gradients of $\bar{\mathbf{u}}_D$
Pr	ν_f/α_f, Prandtl number
r	radius
R	r_o/r_i
Ra_f	$Ra_f = \frac{g\beta r_i^3\Delta T}{\nu_f\alpha_f}$, fluid Rayleigh number
Ra_m	$Ra_m = Ra_f\cdot Da = \frac{g\beta_\phi r_i\Delta TK}{\nu_f\alpha_{eff}}$, Darcy–Rayleigh number
Ra_{cr}	critical Rayleigh number
Re_p	$Re_p = \frac{\lvert\mathbf{u}_D\rvert d}{\nu_f}$, Reynolds number based on the pore diameter
T	temperature
$\mathbf{u}$	microscopic velocity
$\mathbf{u}_D$	Darcy or superficial velocity (volume average of $\mathbf{u}$)

Greek symbols

α	thermal diffusivity
β	thermal expansion coefficient
ΔV	representative elementary volume
ΔV_f	fluid volume inside ΔV
ε	$\varepsilon = \mu\overline{\nabla\mathbf{u}' : (\nabla\mathbf{u}')^T}/\rho$, dissipation rate of k
μ	dynamic viscosity
μ_t	microscopic turbulent viscosity
μ_{t_ϕ}	macroscopic turbulent viscosity
ν	kinematic viscosity
ρ	density
σ's	non-dimensional constants
ϕ	$\phi = \Delta V_f/\Delta V$, porosity
θ	angle

Special characters

φ	general scalar variable
$\bar{\varphi}$	time average
φ'	time fluctuation
$\langle\varphi\rangle^i$	intrinsic average
$\langle\varphi\rangle^v$	volume average
${}^i\varphi$	spatial deviation
$\lvert\varphi\rvert$	absolute value (Abs)
$\boldsymbol{\varphi}$	general vector variable
φ_{eff}	effective value, $\varphi_{eff} = \phi\varphi_f + (1-\phi)\varphi_s$
$\varphi_{s,f}$	solid/fluid
$\varphi_{i,o}$	inner/outer
$\varphi_{H,C}$	hot/cold
φ_ϕ	macroscopic value
$(\ )^T$	transpose

the heated inner cylinder suppresses any movement and turbulence that might be convected downward. *Direct numerical simulation* (DNS) was performed by [9]. However, because of the extreme requirements for computing resources, these computations are limited to low Ra_f numbers. The work of [10] use a *Large Eddy Simulation* (LES) for a case with a high Ra_f number indicated that this method may serve in the future as an alternative to the (DNS), but there are many critics about the use of such model in 2-D cases due the 3-D characteristic of the turbulence. The work of [11], reports on the modeling and computational study of the natural convection in concentric and eccentric annuli by means of several variants of the Algebraic Stress Models (ASM), which is based on the expression for turbulent heat flux $\overline{\theta u_i}$ obtained by truncation of the second-moment transport equation for this correlation. Various levels of closure included the Low-*Re* number form of the k–ε model, but also a version in which the differential transport equations are solved for the temperature variance $\overline{\theta^2}$ and its decay rate ε_θ. Ascending flows of liquid metal [12] and anisotropic effects in flows over rod-bundles, [13] have also been investigated via ASMs.

The natural convection in cylindrical annular geometry filled with porous material also have been studied by distinct numerical approaches, such as the finite-difference method reported by [14 and 15]. Finite element method is found in the work of [16] and the Galerkin spectral method in the work of [17–20]. The work of [21] have shown that the Fourier–Chebyshev method gives better accuracy than

does the full Fourier–Galerkin method for the description of two-dimensional multicellular flows.

Experimental studies using the Christiansen effect to visualize the thermal two-dimensional fields have been carried out by [22]. In contrast with analytical studies, experiments have only unveiled unicellular flows.

Macroscopic transport modeling of incompressible flows in porous media has been based on the volume-average methodology for either heat [23] or mass transfer [24–26]. If time fluctuations of the flow properties are also considered, in addition to spatial deviations, there are two possible methodologies to follow in order to obtain macroscopic equations: (a) application of time-average operator followed by volume-averaging [27–30], or (b) use of volume-averaging before time-averaging is applied [31–33]. However, both sets of macroscopic mass transport equations are equivalent when examined under the recently established *double decomposition* concept [34–38]. The mathematical proof of this statement is demonstrated in [35] and considers that the two additional drag terms that appear in the momentum equation, namely the viscous and form drags, have identical final forms after application of both operators over their exact expressions. Also, in [34–38] no association is made between turbulence and closure of such two drag terms, namely the Darcy and Forcheimer models. Turbulence is handled after "double-decomposing" the convection term (not the drag terms) and setting up models for the additional correlations obtained. To the interested reader the discussions in Refs. [34–38] are suggested for further study.

In addition to considering the flow variables in [34–38], the double-decomposition concept has been extended to heat transfer in [39,40]. Also, a consistent program of systematic studies based on such *double-decomposition idea* for treating buoyant flows [41–44], mass transfer [45], non-equilibrium heat transfer [46,47], double diffusion [48], flow about an interface including mean [49] and turbulence fields [51,52], in addition to a general classification of models [53], have been published. Further applications of the work in [34–38] include flow trough porous inserts [54] and heat transfer in permeable baffles [55].

Motivated by the innumerous practical applications of turbulent natural convection in porous media, and by the fact studies on this subject are not common in the available literature, this paper presents results for both laminar and turbulent flows in a porous layer bounded by two horizontal isothermal concentric cylinders. The turbulence model here adopted is the macroscopic k–ε model developed and applied by de Lemos and co-workers [34–55].

2. The problem considered

The problem considered is showed schematically in Fig. 1a and refers to a concentric annulus completely filled with porous material with outer and inner radii r_o and r_i, respectively, and $R = r_o/r_i = 2$. The cavity is isothermally heated from the inner cylinder, T_H and cooled from outer cylinder, T_C and the parameters Prandtl number, Pr, conductivity ratio, k_s/k_f are fixed.

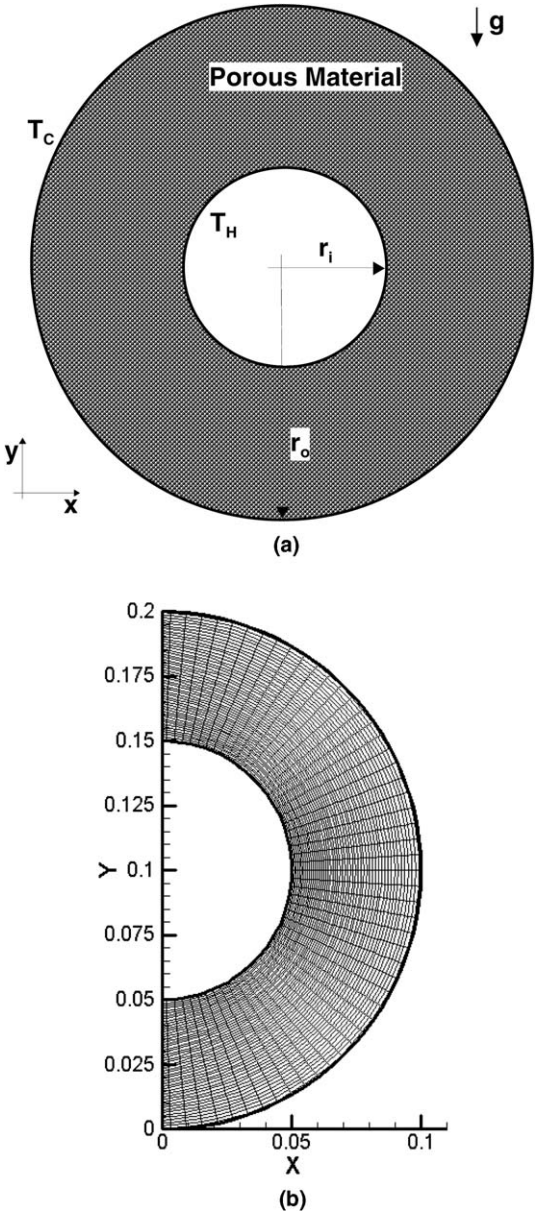

Fig. 1. Schematic of the problem: (a) geometry; (b) grid.

The local Nusselt number on the heated inner cylinder for the horizontal cylindrical annuli considering half domain is given by,

$$Nu = -\ln R \left(r \frac{\partial \langle T \rangle^{i}}{\partial r} \right)_{r=r_i} \tag{1}$$

so that the average Nusselt number becomes,

$$\overline{Nu} = -\frac{\ln R}{\pi} \int_0^{\pi} \left(r \frac{\partial \langle T \rangle^{i}}{\partial r} \right)_{r=r_i} \mathrm{d}\theta \tag{2}$$

The Ra_m is the dimensionless parameter used for porous media and it is defined as, $Ra_m = \frac{g\beta_\phi r_i \Delta T K}{\nu_f \alpha_{eff}}$, with $\alpha_{eff} = k_{eff}/(\rho c_p)_f$ and the medium permeability proposed by [56] and based on the empirical correlations of [57] as $K = \frac{D_p^2 \phi^3}{144(1-\phi)^2}$.

3. Governing equations

The equations used herein are derived in details in Refs. [34–38] and for this reason their derivation need not be repeated here. It is interesting to point out that the value of porosity, ϕ, in the governing equations to be shown below, is located inside the spatial operator (gradient). As such, no assumption is made on the constancy of ϕ over the domain of calculation. The work of [35] points out that the only restriction to apply is the constancy of ϕ with time, otherwise, volume and time average operators do not commute.

Basically, for porous media analysis, a macroscopic form of the time-averaged equations is obtained by taking the volumetric mean of the entire equation set [34–38]. In that development, the medium was considered rigid and saturated by an incompressible fluid. Accordingly, for a general fluid property φ the intrinsic and volumetric averages are related through the porosity ϕ as

$$\langle\varphi\rangle^i = \frac{1}{\Delta V_f}\int_{\Delta V_f} \varphi \, dV; \quad \langle\varphi\rangle^v = \phi\langle\varphi\rangle^i; \quad \phi = \frac{\Delta V_f}{\Delta V} \tag{3}$$

where ΔV_f is the volume of the fluid contained in ΔV, the volume of a Representative Elementary Volume (REV). The property φ can then be defined as the sum of $\langle\varphi\rangle^i$ and a term related to its spatial variation within the REV, ${}^i\varphi$, as [25],

$$\varphi = \langle\varphi\rangle^i + {}^i\varphi \tag{4}$$

The macroscopic continuity equation is then given by,

$$\nabla\cdot\bar{\mathbf{u}}_D = 0 \tag{5}$$

where the Dupuit–Forchheimer relationship, $\bar{\mathbf{u}}_D = \phi\langle\bar{\mathbf{u}}\rangle^i$, has been used and $\langle\bar{\mathbf{u}}\rangle^i$ identifies the intrinsic (liquid) average of the local velocity vector $\bar{\mathbf{u}}$. The macroscopic time-mean Navier–Stokes (NS) equation for an incompressible fluid with constant properties is given as,

$$\begin{aligned}\rho\left[\frac{\partial\bar{\mathbf{u}}_D}{\partial t} + \nabla\cdot\left(\frac{\bar{\mathbf{u}}_D\bar{\mathbf{u}}_D}{\phi}\right)\right] &= -\nabla\left(\phi\langle\bar{p}\rangle^i\right) + \mu\nabla^2\bar{\mathbf{u}}_D + \nabla\cdot\left(-\rho\phi\langle\overline{\mathbf{u}'\mathbf{u}'}\rangle^i\right)\\ &\quad - \rho\beta_\phi\mathbf{g}\phi(\langle\bar{T}\rangle^i - T_{ref}) - \left[\frac{\mu\phi}{K}\bar{\mathbf{u}}_D + \frac{c_F\phi\rho|\bar{\mathbf{u}}_D|\bar{\mathbf{u}}_D}{\sqrt{K}}\right]\end{aligned} \tag{6}$$

Before proceeding, a word about the mechanical dispersion mechanism seems timely. Bear [24] and Hsu and Cheng [23] have defined, among others, the dispersion mechanism for momentum and heat transport, respectively. Mathematically speaking, dispersion is a space correlation between deviation of a generic flow property and velocity deviation (see [35]). When the flow property is velocity, temperature, or mass concentration, one has *mechanical*, *thermal* or *mass* dispersion, respectively. Such mechanism is also present in laminar flow through porous media (low $Re_p = |\mathbf{u}_D|d/\nu_f$).

In addition, to better clarify matters, one recalls that from [35] the full decomposition of the convection term, applying the double-decomposition concept, rendered four terms (rather than two for either time decomposition only or space decomposition only), which were given the following physical significance (see [35] for details): (a) *convection*, $\nabla\cdot(\rho\phi\langle\bar{\mathbf{u}}\rangle^i\langle\bar{\mathbf{u}}\rangle^i)$, (b) *mechanical dispersion*, $\nabla\cdot(\rho\phi\langle{}^i\bar{\mathbf{u}}{}^i\bar{\mathbf{u}}\rangle^i)$, which is also present in laminar flows, $Re_p < 150$, (c) *macroscopic turbulent transport*, $\nabla\cdot(\rho\phi\overline{\langle\mathbf{u}'\rangle^i\langle\mathbf{u}'\rangle^i})$ and (d) *turbulent dispersion*, $\nabla\cdot(\rho\phi\langle\overline{{}^i\mathbf{u}'{}^i\mathbf{u}'}\rangle^i)$. Having defined an appropriate nomenclature, considerations about characteristics of the models here employed can be made.

In view of the above, it is interesting to point out that mechanical dispersion, or term (b) above, $\nabla\cdot(\rho\phi\langle{}^i\bar{\mathbf{u}}{}^i\bar{\mathbf{u}}\rangle^i)$, has been neglected in (6) in comparison to the other three mechanisms. The reason for assuming such hypothesis is that this work in intended to model high *Re* flows in highly permeable, high porosity media, for which the corresponding range of pore Reynolds number is given by $Re_p > 300$, provided that porosity and pore diameters are high. As such, turbulent flow is assumed to exist within the medium and, under this condition, turbulent transfer (third term on the right of (6)), given by,

$$\nabla\cdot(-\rho\phi\langle\overline{\mathbf{u}'\mathbf{u}'}\rangle^i) = \nabla\cdot\left[-\rho\phi\left(\underbrace{\overline{\langle\mathbf{u}'\rangle^i\langle\mathbf{u}'\rangle^i}}_{\substack{\text{macroscopic}\\ \text{turb. transp.}}} + \underbrace{\langle\overline{{}^i\mathbf{u}'{}^i\mathbf{u}'}\rangle^i}_{\substack{\text{turbulent}\\ \text{dispersion}}}\right)\right] \tag{7}$$

overwhelms mechanical dispersion (see [35]). For laminar flow with low Re_p, however, the greater importance of mechanical dispersion as an effective mechanism of momentum exchange is commonly accepted in the literature. On should point out though that *thermal* dispersion is here not neglected, as will be seen below.

Further, when treating turbulence with statistical tools, the correlation $-\rho\overline{\mathbf{u}'\mathbf{u}'}$ appears after application of the time-average operator to the local instantaneous NS equation. Applying further the volume-average procedure to this correlation results in the term $-\rho\phi\langle\overline{\mathbf{u}'\mathbf{u}'}\rangle^i$. This term is here recalled the *Macroscopic Reynolds Stress Tensor* (MRST). Further, a model for the (MRST) in analogy with the Boussinesq concept for clear fluid can be written as:

$$-\rho\phi\langle\overline{\mathbf{u}'\mathbf{u}'}\rangle^i = \mu_{t_\phi} 2\langle\bar{\mathbf{D}}\rangle^v - \frac{2}{3}\phi\rho\langle k\rangle^i\mathbf{I} \tag{8}$$

where

$$\langle\bar{\mathbf{D}}\rangle^v = \frac{1}{2}\left[\nabla(\phi\langle\bar{\mathbf{u}}\rangle^i) + \left[\nabla(\phi\langle\bar{\mathbf{u}}\rangle^i)\right]^T\right] \tag{9}$$

is the macroscopic deformation rate tensor, $\langle k\rangle^i$ is the intrinsic average for k and μ_{t_ϕ} is the macroscopic turbulent viscosity. The macroscopic turbulent viscosity, μ_{t_ϕ}, is

modeled similarly to the case of clear fluid flow and a proposal for it was presented in [35] as,

$$\mu_{t_\phi} = \rho c_\mu \frac{\langle k\rangle^{i^2}}{\langle \varepsilon\rangle^{i}} \tag{10}$$

In a similar way, applying both time and volumetric average to the microscopic energy equation, for either the fluid or the porous matrix, two equations arise. Assuming further the *Local Thermal Equilibrium Hypothesis*, which considers $\langle \overline{T}_f\rangle^i = \langle \overline{T}_s\rangle^i = \langle \overline{T}\rangle^i$, and adding up these two equations, one has,

$$\begin{aligned}&(\rho c_p)_f \nabla\cdot(\phi\langle \overline{\mathbf{u}T}_f\rangle^i)\\ &\quad = (\rho c_p)_f \nabla\cdot\left\{\phi(\langle\bar{\mathbf{u}}\rangle^i\langle\overline{T}_f\rangle^i + \overline{\langle\mathbf{u}'\rangle^i\langle T'_f\rangle^i} + \langle{}^i\bar{\mathbf{u}}^i\overline{T}_f\rangle^i + \langle\overline{{}^i\mathbf{u}'^i T'_f}\rangle^i)\right\}\end{aligned} \tag{11}$$

A modeled form of (11) has been given in detail in the work of [40] as,

$$\begin{aligned}&\{(\rho c_p)_f\phi + (\rho c_p)_s(1-\phi)\}\frac{\partial\langle\overline{T}\rangle^i}{\partial t} + (\rho c_p)_f\nabla\cdot(\bar{\mathbf{u}}_D\langle\overline{T}\rangle^i)\\ &\quad = \nabla\cdot\{\mathbf{K}_{eff}\cdot\nabla\langle\overline{T}\rangle^i\}\end{aligned} \tag{12}$$

where $\mathbf{K}_{eff}$, given by

$$\mathbf{K}_{eff} = [\phi k_f + (1-\phi)k_s]\mathbf{I} + \mathbf{K}_{tor} + \mathbf{K}_t + \mathbf{K}_{disp} + \mathbf{K}_{disp,t} \tag{13}$$

is the effective conductivity tensor. In order to be able to apply (12), it is necessary to determine the conductivity tensors in (13), *i.e.*, $\mathbf{K}_{tor}$, $\mathbf{K}_t$, $\mathbf{K}_{disp}$ and $\mathbf{K}_{disp,t}$. Following [29], this can be accomplished for the *tortuosity* and *thermal dispersion* conductivity tensors, $\mathbf{K}_{tor}$ and $\mathbf{K}_{disp}$, by making use of a unit cell subjected to periodic boundary conditions for the flow and a linear temperature gradient imposed over the domain. The conductivity tensors are then obtained directly from the microscopic results for the unit cell.

As mentioned earlier, here, *thermal* dispersion is not neglected. Kuwahara and Nakayama [29] present, for an infinite medium formed by an array of square rods, the $\mathbf{K}_{disp}$ components in the longitudinal and transversal directions, $(\mathbf{K}_{disp})_{XX}$ and $(\mathbf{K}_{disp})_{YY}$, respectively. The expressions read,

$$\begin{aligned}(K_{disp})_{XX} &= \begin{cases} 0.022\frac{Pe_D^2}{(1-\phi)}k_f, & Pe_D < 10\\ 2.7\frac{Pe_D}{\phi^{1/2}}k_f, & Pe_D > 10\end{cases}\\ (K_{disp})_{YY} &= \begin{cases} 0.022\frac{Pe_D^{1.7}}{(1-\phi)^{1/4}}k_f, & Pe_D < 10\\ 0.052(1-\phi)^{1/2}Pe_D k_f, & Pe_D > 10\end{cases}\end{aligned} \tag{14}$$

where

$$Pe_D = Pe(1-\phi)^{1/2};\quad Pe = Re_p Pr;\quad Re_p = \frac{|\mathbf{u}_D|d}{\nu_f} \tag{15}$$

and d is the pore diameter. The use of unit cells to obtain correlations (14) is based on the notion that, for an infinite medium, the macroscopic flow is "fully developed" (see also [36–38]). Within the cell, after applying periodic boundary conditions at cell inlet and outlet, one can then compute distributed flow quantities that can be used to calculate volumetric averages and spatial deviations. As such, correlations composing the dispersion terms can be numerically evaluated. This situation is akin to the determination of constants in statistical turbulence models. One has to isolate individual transport mechanisms in order to focus on specific term and then "calibrate" or adjust some proposed constant. Clearly, correlations (14) would be only exact for flows where the macroscopic fully developed condition applies. Nevertheless, in the absence of better information, its application to general flows should be seen as an approximation, which is subjected to refinement as more experimental data is gathered.

The turbulent heat flux and turbulent thermal dispersion terms, $\mathbf{K}_t$ and $\mathbf{K}_{disp,t}$, which cannot be determined from such a microscopic calculation, are modeled here through the Eddy diffusivity concept, similarly to [30]. It should be noticed that these terms arise only if the flow is turbulent, whereas the tortuosity and the thermal dispersion terms exist for both laminar and turbulent flow regimes. Starting out from the time averaged energy equation coupled with the microscopic modeling for the 'macroscopic turbulent heat flux' through the Eddy diffusivity concept, one can write, after volume averaging,

$$-(\rho c_p)_f\langle\overline{\mathbf{u}'T'_f}\rangle^i = (\rho c_p)_f\frac{\nu_{t_\phi}}{\sigma_T}\nabla\langle\overline{T}_f\rangle^i \tag{16}$$

where the symbol ν_{t_ϕ} expresses the macroscopic Eddy viscosity, $\mu_{t_\phi} = \rho_f\nu_{t_\phi}$, given by (10) and σ_T is a constant. According to (16), the macroscopic heat flux due to turbulence is taken as the sum of the turbulent heat flux and the turbulent thermal dispersion found by [40]. In view of the arguments given above, the *turbulent heat flux* and *turbulent thermal dispersion* components of the conductivity tensor, $\mathbf{K}_t$ and $\mathbf{K}_{disp,t}$, respectively, are expressed as:

$$\mathbf{K}_t + \mathbf{K}_{disp,t} = \phi(\rho c_p)_f\frac{\nu_{t_\phi}}{\sigma_T}\mathbf{I} \tag{17}$$

In the equation set shown above, when the variable $\phi = 1$, the domain is considered as a clear medium. For any other value of ϕ, the domain is treated as a porous medium.

3.1. Turbulence model

Transport equations for $\langle k\rangle^i = \langle\overline{\mathbf{u}'\cdot\mathbf{u}'}\rangle^i/2$ and $\langle\varepsilon\rangle^i = \mu\langle\overline{\nabla\mathbf{u}':(\nabla\mathbf{u}')^T}\rangle^i/\rho$ in their so-called High Reynolds number form are fully documented in the works of [34–38] making use of the *Double Decomposition* concept and extended in [41] to incorporate buoyancy effects. Basically, for porous media analysis, a macroscopic form of the governing equations is here obtained by taking the volumetric average of the time averaged equations set.

As explained in [35], different paths in obtaining a k-equation have been proposed. The works of [31,32] developed a macroscopic equation for the turbulent kinetic energy formed as $k_m = \overline{\langle\mathbf{u}'\rangle^i\cdot\langle\mathbf{u}'\rangle^i}/2$, whereas de Lemos

and co-workers [34–55] based their model on $\langle k\rangle^{\mathrm{i}} = \overline{\langle \mathbf{u}'\cdot\mathbf{u}'\rangle^{\mathrm{i}}}/2$. The relationship between these two quantities is [34]

$$\langle k\rangle^{\mathrm{i}} = \overline{\langle \mathbf{u}'\cdot\mathbf{u}'\rangle^{\mathrm{i}}}/2 = \overline{\langle \mathbf{u}'\rangle^{\mathrm{i}}\cdot\langle \mathbf{u}'\rangle^{\mathrm{i}}}/2 + \overline{\langle {}^{\mathrm{i}}\mathbf{u}'\cdot{}^{\mathrm{i}}\mathbf{u}'\rangle}/2 = k_m + \overline{\langle {}^{\mathrm{i}}\mathbf{u}'\cdot{}^{\mathrm{i}}\mathbf{u}'\rangle}/2 \tag{18}$$

For that reason, transport equations for $k_m = \overline{\langle \mathbf{u}'\rangle^{\mathrm{i}}\cdot\langle \mathbf{u}'\rangle^{\mathrm{i}}}/2$ and $\langle k\rangle^{\mathrm{i}} = \overline{\langle \mathbf{u}'\cdot\mathbf{u}'\rangle^{\mathrm{i}}}/2$ are not equal because, as seen, they represent two different quantities being transported [34]. In this work, macroscopic turbulent transport equations are given by [41]:

$$\rho\left[\frac{\partial}{\partial t}(\phi\langle k\rangle^{\mathrm{i}}) + \nabla\cdot(\bar{\mathbf{u}}_{\mathrm{D}}\langle k\rangle^{\mathrm{i}})\right] = \nabla\cdot\left[\left(\mu + \frac{\mu_{\mathrm{t}_\phi}}{\sigma_k}\right)\nabla(\phi\langle k\rangle^{\mathrm{i}})\right] + P^i + G^i + G^{\mathrm{i}}_\beta - \rho\phi\langle\varepsilon\rangle^{\mathrm{i}} \tag{19}$$

$$\rho\left[\frac{\partial}{\partial t}(\phi\langle \varepsilon\rangle^{\mathrm{i}}) + \nabla\cdot(\bar{\mathbf{u}}_{\mathrm{D}}\langle \varepsilon\rangle^{\mathrm{i}})\right] = \nabla\cdot\left[\left(\mu + \frac{\mu_{\mathrm{t}_\phi}}{\sigma_\varepsilon}\right)\nabla(\phi\langle \varepsilon\rangle^{\mathrm{i}})\right] + c_1P^i\frac{\langle\varepsilon\rangle^{\mathrm{i}}}{\langle k\rangle^{\mathrm{i}}} + c_2\frac{\langle\varepsilon\rangle^{\mathrm{i}}}{\langle k\rangle^{\mathrm{i}}}G^i + c_1c_3G^{\mathrm{i}}_\beta\frac{\langle\varepsilon\rangle^{\mathrm{i}}}{\langle k\rangle^{\mathrm{i}}} - c_2\rho\phi\frac{\langle\varepsilon\rangle^{i^2}}{\langle k\rangle^{\mathrm{i}}} \tag{20}$$

where c_1, c_2, c_3 and c_k are constants, $P^i\left(=-\rho\langle\overline{\mathbf{u}'\mathbf{u}'}\rangle^{\mathrm{i}}:\nabla\bar{\mathbf{u}}_{\mathrm{D}}\right)$ is the production rate of $\langle k\rangle^{\mathrm{i}}$ due to gradients of $\bar{\mathbf{u}}_{\mathrm{D}}$, $G^i\left(=c_k\rho\frac{\phi\langle k\rangle^{\mathrm{i}}|\bar{\mathbf{u}}_{\mathrm{D}}|}{\sqrt{K}}\right)$ is the generation rate of the intrinsic average of k due to the action of the porous matrix and $G^{\mathrm{i}}_\beta\left(=\phi\frac{\mu_{\mathrm{t}_\phi}}{\sigma_{\mathrm{t}}}\beta_\phi\mathbf{g}\cdot\nabla\langle\overline{T}\rangle^{\mathrm{i}}\right)$ is the generation rate of $\langle k\rangle^{\mathrm{i}}$ due to the buoyant effects. Here, it is also important to emphasize that mechanical dispersion was not considered in the transport of $\langle k\rangle^{\mathrm{i}}$ and $\langle\varepsilon\rangle^{\mathrm{i}}$, as was the case for the mean momentum Eq. (6). For highly porous and permeable media, for a fluid flowing with a high value of Re_{p}, turbulence interactions are expected to transport momentum and turbulent kinetic energy as a rate faster than that due to dispersion mechanisms.

Further, the constants used in Eqs. (10), (19) and (20) of the macroscopic k–ε model were the same given in [58] for clear medium ($\phi = 1$ and $K\to\infty$). They read,

$$c_\mu = 0.09,\quad c_1 = 1.44,\quad c_2 = 1.92,\quad c_3 = 1.0,\quad \sigma_k = 1.0,\quad \sigma_\varepsilon = 1.3,\quad \sigma_T = 0.9 \tag{21}$$

For a porous medium, these constants may present different values but, as a first approximation, they were taken as equal to those in [58], as suggested in [31].

Further, standard wall function has been employed for calculating the flow near to the walls, as discussed in [49]. The use of such simpler model is justified due to the final velocity values close to the interface will be a function not only of inertia and viscous effects in full Navier–Stokes equation, but also due to the Darcy and Forchheimer resistance terms. Therefore, eventual errors coming from inaccurate use of more appropriate boundary conditions will have little influence on the final value for velocity close to the wall since drag forces, caused by the porous structure, will play also an important role in determining the final value for the wall velocity. Thus, logarithm wall laws are simple to be incorporated when simulating flow over rigid surfaces and for that they have been modified to include surface roughness and to simulate flows over irregular surfaces at the bottom of rivers [59]. Detailed information on such numerical treatment can be found in [35–37].

4. Numerical method and solution procedure

The numerical method employed for discretizing the governing equations is the control-volume approach with a generalized grid. A hybrid scheme, Upwind Differencing Scheme (UDS) and Central Differencing Scheme (CDS), is used for interpolating the convection fluxes. The well-established SIMPLE algorithm [60] is followed for handling the pressure-velocity coupling. Individual algebraic equation sets were solved by the SIP procedure of [61]. In addition, concentration of nodal points closer to the walls reduces eventual errors due to numerical diffusion which, in turn, are further annihilated due to the hybrid scheme here adopted.

5. Results and discussion

In order to guarantee grid independent solutions, runs were performed in grids up to 80×80 control volumes for laminar flow with $Ra_{\mathrm{m}} = 500$. The percent difference of the averaged Nusselt number at the hot wall, compared with results obtained with the 50×50 grid, is less than 1%. Therefore, the 50×50 mesh seems to be refined enough near to the walls to capture the thin boundary layers that appear along the vertical surfaces.

5.1. Laminar model solution

Runs for laminar model solution were performed with a 50×50 control volumes in the grid shown in Fig. 1b. The present results were obtained with $\phi = 0.2$ (to represent the packed bed measured by Caltagirone [14]) and $\phi = 0.8$, Prandtl number, $Pr = 7$ and the conductivity ratio between the solid and fluid phases are assumed to be a unit (unless otherwise noted).

As pointed out in [42 and 62] for the non-Darcy region, fluid flow and heat transfer in porous cavities depend on the fluid Rayleigh number, Ra_{f}, and the Darcy number, Da, when other parameters such as ϕ, Pr, $k_{\mathrm{f}}/k_{\mathrm{s}}$ are fixed. Therefore, porosity, Prandtl number and conductivity ratio were here kept fixed. It is also important to emphasize that most of runs were performed without the contribution of the thermal dispersion, $\mathbf{K}_{\mathrm{disp}}$. However, a few cases considering the effect of thermal dispersion on the Nusselt number were also computed in order to show its influence on the overall heat transport.

Many workers have focused their attention on the bifurcation and stability of the numerical solution. This work has not this intention and its objective is to validate the numerical tool comparing the present results with others numerical and experimental works.

According to [14], there are three convection regimes when considered the horizontal cylindrical annuli filled with porous material. The first is for $Ra_m \leqslant 8$ and the convective phenomena are very little developed and the heat transfer process occurs only by conduction mechanism. This regime is called *pseudo-conduction*. The second regime lies in the range $8 < Ra_m < 65$ and the convective phenomena is considered to be steady. The fluid is heated on contact with the inner cylinder and impinges onto to the outer surface. The last regime is for $Ra_m > 65$, which is characterized by flow perturbations in the upper part of the annular layer causing fluctuations in temperature.

Further, experimental observations suggest that, for high Rayleigh numbers, the fluid flow domain can be divided into five regions. According to [20], the first region is the *Inner boundary layer* which has a thin thermal layer close to the inner cylinder where the gradients in the angular direction are negligible compared to those in the radial direction. The second is the *Outer boundary layer* with a thin thermal layer near the outer cylinder in which gradients in the angular direction are also negligible compared to those in the radial direction. The third region is the *Plume* that exits along the vertical line of symmetry above the inner cylinder and joins the inner and outer thermal layers. The fourth region is the *Stagnant region*, which is located below the inner cylinder where buoyancy forces inhibits fluid motion and heat transfer is transferred purely by conduction mechanism. At last, the *Core region* is the one bounded by the other four regions. Having described the basic features of the flow structure, numerical results are now presented.

First, to validate the code, Table 1 compares some previous [14,18] and present laminar results for $25 < Ra_m < 500$ and $\phi = 0.2$. This low porosity value was chosen in order to represent the packed bed composed by glass balls of $D_p = 3$ mm used in [14]. Computations are for $Da = 3.125 \times 10^{-7}$ $(K = 0.7813 \times 10^{-9}\ \mathrm{m}^2)$, $k_s/k_f = 1$, $Pr = 7$ (water) and $\mathbf{K}_{disp} = 0$. Table 1 shows a good agreement between the present and previous results in the literature. Fig. 2 further shows the behavior of the average Nusselt number versus Ra_m from experiments and other analyses. The present results in Fig. 2 were obtained with the laminar model for $R = 2$ and applying the conditions show in Table 1, which were used by (14). Such parameters try to reproduce the experimental conditions carried out in [14], which considered water and glass balls of 3 and 4 mm in diameter. Present laminar results in Fig. 2 show a good agreement with respect to the numerical tool used in [14] but, however, experimental values are a little higher for high values of Ra_m. The figure also indicates an improvement on the simulations when the mechanism of dispersion is considered. A possible explanation for the under predicted values for high Ra_m could be associated with the three-dimensional characteristics of the real flow and additional mechanisms, such as turbulence, not accounted for in the predictions shown in Fig. 2.

Table 1
Some previous laminar numerical results for average Nusselt number for Ra_m ranging from 25 to 500 with $K = 0.7813 \times 10^{-9}\ \mathrm{m}^2$, $D_p = 3$ mm, $Da = 3.125 \times 10^{-7}$, $k_s/k_f = 1$, $\phi = 0.2$, $Pr = 7$, $\mathbf{K}_{disp} = 0$

	Ra_m				
	25	100	150	200	500
Caltagirone [14]	1.0993	1.8286	–	2.6256	4.1983
Charrier-Mojtabi [18]	–	1.8670	2.3090	–	–
Present results, $\mathbf{K}_{disp} = 0$	1.1095	1.8629	2.3023	2.6764	4.2741
Present results, $\mathbf{K}_{disp}$ by Eq. (14)	1.1103	1.8783	2.3413	2.7500	4.7439

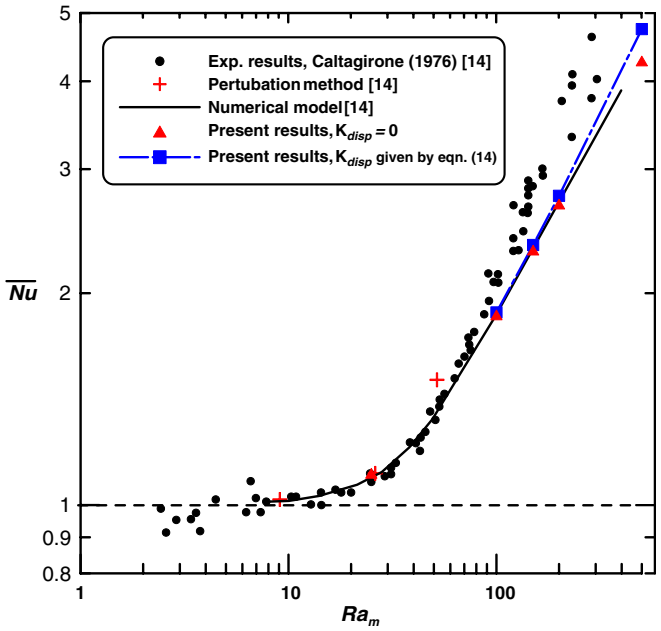

Fig. 2. Behavior of the average Nusselt number versus Rayleigh number, laminar model, Ra_m, with $R = 2$, $K = 0.7813 \times 10^{-9}\ \mathrm{m}^2$, $D_p = 3$ mm, $Da = 3.125 \times 10^{-7}$, $k_s/k_f = 1$, $\phi = 0.2$, $Pr = 7$ and $\mathbf{K}_{disp}$ given by (14).

Fig. 3 shows streamlines and isotherms for laminar model solution for a cylindrical porous annuli with $Da = 3.125 \times 10^{-7}$, $k_s/k_f = 1$, $\phi = 0.2$, $Pr = 7$ and Ra_m ranging from 25 to 500. The cavity is heated at the inner cylindrical surface and cooled from the outer cylinder.

For lower Rayleigh number values, $Ra_m \leqslant 25$ (not shown here), the isotherms are concentric to the inner cylinder, indicating that the most part of heat transfer is due to conduction mechanism, while the streamlines yield a recirculation bubble located at each half of the annulus. Fig. 3a,b and e,f show a good agreement when compared with those figures from the work of [14, pp. 346 and 350] for $Ra_m = 25$ and $Ra_m = 200$, respectively.

The heat transfer coefficient is seen to increase as the Rayleigh number is varied distorting the circular isotherms and creating a plume above the inner cylinder as convection becomes dominant (see Fig. 3b and h). Streamlines do not

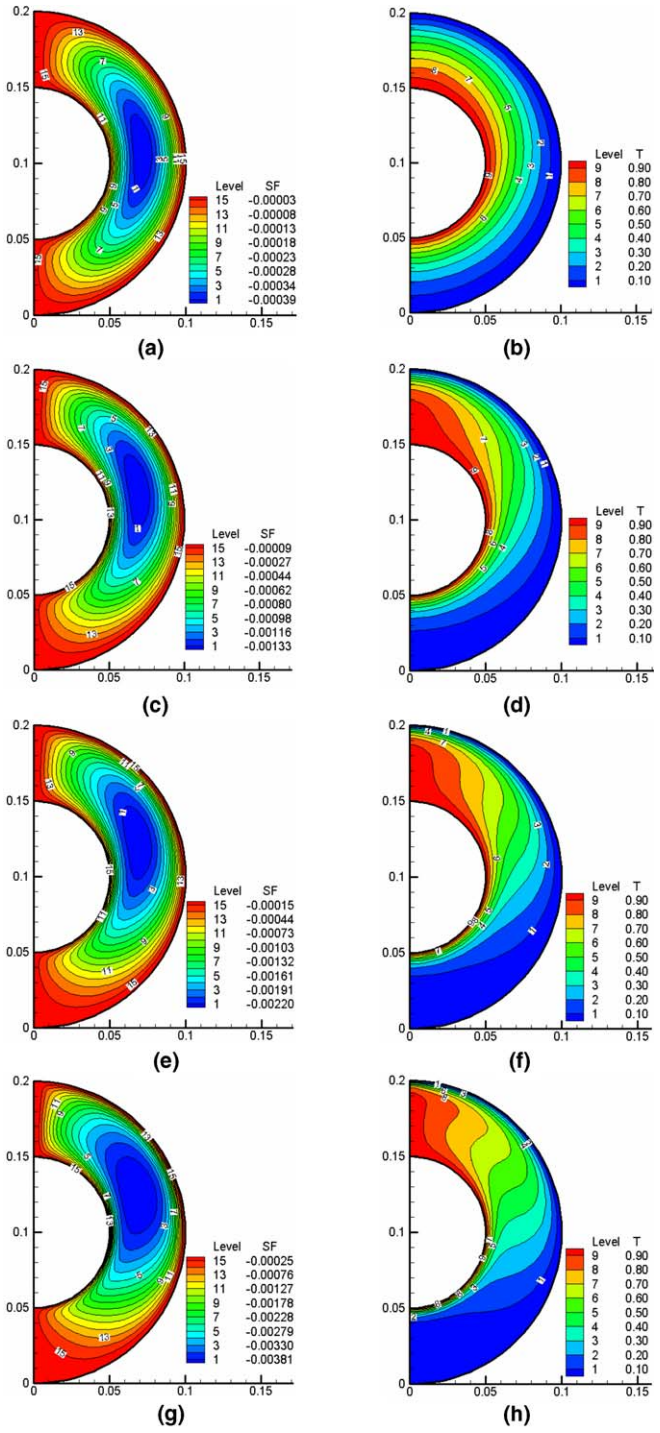

Fig. 3. Streamlines (left) and isotherms (right) for laminar model solution for a cylindrical porous annuli with $R = 2$, $D_p = 3$ mm, $Da = 3.125 \times 10^{-7}$, $k_s/k_f = 1$, $\phi = 0.2$, $Pr = 7$, $\mathbf{K}_{disp} = 0$, (a, b) $Ra_m = 25$, (c, d) $Ra_m = 100$, (e, f) $Ra_m = 200$ and (g, h) $Ra_m = 500$.

present such intense variations in shape as the Rayleigh number is varied but only an increase in the recirculation strength and a slight displacement of the vortex center towards the upper part of the annulus (see Fig. 3a and g).

Table 2 further shows the average Nusselt number for different Darcy numbers for Ra_m ranging from 25 to 500 and $\phi = 0.8$. It is clearly seen from the (2) that for a fixed

Table 2
Behavior of the average Nusselt number for different values of Da for Ra_m ranging from 25 to 500 with $k_s/k_f = 1$, $\phi = 0.8$, $Pr = 7$, ($\mathbf{K}_{disp} = 0$, unless otherwise noted)

Da	Ra_m				
	25	100	150	200	500
3.2×10^{-4}	1.0836	1.7042	2.0560	2.3468	3.4797
3.2×10^{-4}, $\mathbf{K}_{disp}$ given by Eq. (14)	1.0907	1.7503	2.1642	2.5374	4.4075
3.2×10^{-5}	1.1035	1.8243	2.2395	2.5889	4.0277
3.2×10^{-6}	1.1090	1.8581	2.2936	2.6635	4.2295

Ra_m that the lower the permeability, and consequently the lower the Da number, the higher the average Nusselt number at the hot wall. This trend has been also observed in [42] and is due to the constraint of having the definition $Ra_m = Ra_f Da$. Different combinations of Ra_f and Da yields different heat transfer results although the value of Ra_m is kept constant. Accordingly, increasing the fluid Rayleigh number, as Da is reduced, enhances natural convection inside the annulus. As pointed out in [42], if Ra_m is fixed, a higher fluid Rayleigh number is associated with a less permeable media (*i.e.*, having a lower Darcy number). It is also clearly seen from the Table 2 that the Nusselt numbers computed with the thermal dispersion mechanism are higher than those computed without $\mathbf{K}_{disp}$ (see Table 2 for $Da = 3.2 \times 10^{-4}$). It seems evident then that this additional mechanism also increases heat transfer. Table 2 further shows that for higher values of Ra_m, the effect of the thermal dispersion on the Nusselt number are more pronounced. For example, including $\mathbf{K}_{disp}$ for $Ra_m = 25$ increases Nu by only $100 \times (1.0907 - 1.0836)/1.0836 = 0.65\%$ whereas for Ra_m equal to 500 such increase is $100 \times (4.4075 - 3.4797)/3.4797 = 26.75\%$. However, although not shown here, the computational cost due to the inclusion of this mechanism significantly rises.

5.2. Turbulence model solution

In this work, the same strategy used in [42] is adopted. First, the turbulence model is switched off and the laminar branch of the solution is obtained when increasing the Rayleigh number, Ra_m. Subsequently, the turbulence model is included and calculations start at high Ra_m, merging to the laminar branch for a reducing Ra_m. Using this methodology, a critical Rayleigh number, Ra_{cr}, is sought for which the two branches of the solutions differ by a prescribed percentage. This convergence of results as Ra_m decreases can be seen as an estimate of the so-called *laminarization* phenomenon. Below a critical Ra_m number the standard k–ε model gives a turbulent viscosity that is close to zero everywhere and the solution can be interpreted as an approximation of the laminar flow. However, above this critical value, the turbulent viscosity increases and turbulent flow is considered.

Calculations for turbulent flow were performed with the same grid used for the laminar model solution. The same parameters (porosity, Prandtl number and conductivity

ratio between the fluid and the solid matrix) were also employed when running the k–ε model, whose results are presented in Fig. 4. Comparing the laminar and the turbulent solution (Figs. 3 and 4), one can note that for the smallest Ra_m considered, Figs. 3a,b and 4a,b, both cases (laminar and turbulent model solutions) do not show remarkable differences and the flow pattern remains almost the same with the center of the streamlines a little further downward for the turbulent case. For the highest Ra_m number analyzed, the isotherms presented in Fig. 4h in the region located beneath the inner cylinder show a similar behavior when compared with those from the laminar case, in which the buoyancy forces inhibits fluid motion and the heat transfer is purely by conduction mechanism, Fig. 3h. However, the upper part of the annulus in Fig. 4h does not show a plume above the inner heated cylinder as appears in the laminar case of Fig. 3h.

Accordingly, Fig. 5a shows the corresponding macroscopic temperature profiles at the symmetry line above the inner cylinder for $Ra_m = 500$, $R = 2$, $Da = 3.2 \times 10^{-5}$, $k_s/k_f = 1$, $\phi = 0.8$, $Pr = 7$, $\mathbf{K}_{disp} = 0$ for laminar and turbu-

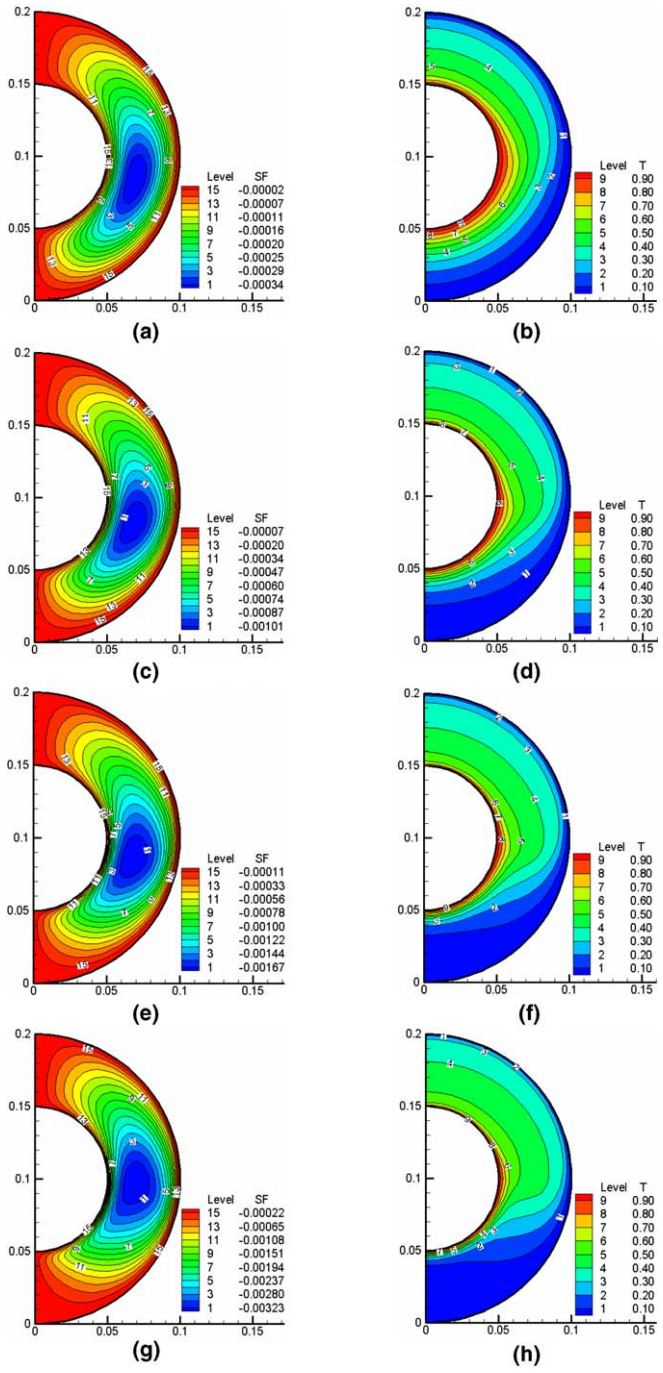

Fig. 4. Streamlines (left) and isotherms (right) for turbulent model solution for a cylindrical porous annuli with $R = 2$, $Da = 3.2 \times 10^{-5}$, $k_s/k_f = 1$, $\phi = 0.8$, $Pr = 7$, $\mathbf{K}_{disp} = 0$, (a, b) $Ra_m = 25$, (c, d) $Ra_m = 100$, (e, f) $Ra_m = 200$ and (g, h) $Ra_m = 500$.

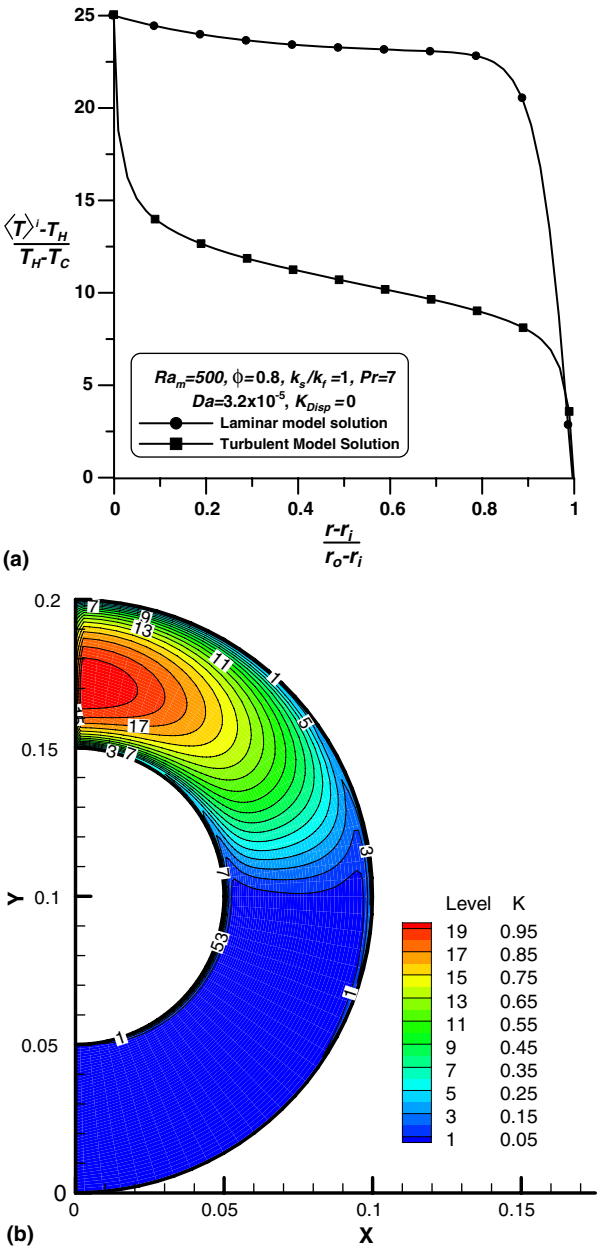

Fig. 5. Laminar and turbulent model solutions for $Ra_m = 500$, $R = 2$, $Da = 3.2 \times 10^{-5}$, $k_s/k_f = 1$, $\phi = 0.8$, $Pr = 7$, $\mathbf{K}_{disp} = 0$: (a) macroscopic temperature behavior at the symmetry line above the inner cylinder; (b) isolines of intrinsic turbulent kinetic energy, $\langle k \rangle^i$.

Table 3
Comparison between laminar and turbulent model solutions for the average Nusselt number at the hot wall for $3.2\times10^{-4} > Da > 3.2\times10^{-6}$ and Ra_m ranging from 25 to 500 with $k_s/k_f = 1$, $\phi = 0.8$, $Pr = 7$, ($\mathbf{K}_{disp} = 0$, unless otherwise noted)

Model solution\Ra_m	25	100	150	200	500
$Da = 3.2\times10^{-6}$					
Ra_f	7.8125×10^{6}	3.125×10^{7}	4.6875×10^{7}	6.25×10^{7}	1.5625×10^{8}
Laminar	1.1090	1.8581	2.2936	2.6635	4.2295
Turbulent	7.0036	11.2417	12.6458	13.6791	16.9869
$Da = 3.2\times10^{-5}$					
Ra_f	7.8125×10^{5}	3.125×10^{6}	4.6875×10^{6}	6.25×10^{6}	1.5625×10^{7}
Laminar	1.1035	1.8243	2.2395	2.5889	4.0277
Turbulent	2.3621	4.4824	5.3780	6.0961	8.8406
$Da = 3.2\times10^{-4}$					
Ra_f	7.8125×10^{4}	3.125×10^{5}	4.6875×10^{5}	6.25×10^{5}	1.5625×10^{6}
Laminar	1.0836	1.7042	2.0560	2.3468	3.4797
Turbulent	1.1415	1.9344	2.3875	2.7638	4.2966
$Da = 3.2\times10^{-4}$, $\mathbf{K}_{disp}$ given by Eq. (14)					
Ra_f	7.8125×10^{4}	3.125×10^{5}	4.6875×10^{5}	6.25×10^{5}	1.5625×10^{6}
Laminar	1.0907	1.7503	2.1642	2.5374	4.4075
Turbulent	1.1445	1.9792	2.4856	2.9302	5.0425

lent model solutions. As indicated by the figure, the turbulent solution shows a more gradual temperature distribution across the entire gap when compared with those for the laminar case. The steeper temperature gradient at the inner wall indicates that more heat is transferred through the gap. Fig. 5b shows corresponding isolines of intrinsic turbulent kinetic energy, $\langle k\rangle^i$, for the same conditions as in Fig. 5a. The figure clearly shows that in the upper part of the annular region the turbulent kinetic energy presents its highest levels. The enhancement of heat transfer across the gap is coherent with the large values for $\langle k\rangle^i$ observed in that same region. These high levels of turbulent kinetic energy promote a higher overall heat flux from the inner surface towards the outer cylinder, reflecting on the shape of the temperature profiles seen before in Fig. 5a.

Table 3 shows, for selected modified Rayleigh numbers $Ra_m = Ra_f Da$, the average Nusselt number $\overline{Nu}$ based on the heated inner cylinder. Also shown in the table are corresponding values for the fluid Raleigh number Ra_f, which increases as Da decreases for maintaining the same Ra_m. In general, the overall turbulent average Nusselt numbers are significantly greater than those obtained with the laminar model. A possible explanation for this Nu behavior is that the thin thermal boundary layer above the inner cylinder, appearing when turbulence is considered (see Fig. 5a), entails a steeper temperature gradient which, in turn, promotes the exchange of heat across the gap. These results seem to be in agreement with all simulations shown so far. Also seen is that by keeping ϕ, Pr and k_s/k_f constants, the lower the Darcy number (or the higher Ra_f), the higher the difference of the average Nusselt numbers between the two models. Table 3 seems to suggest that a lower permeability (or a higher Ra_f) implies in an earlier *laminarization*, *i.e.*, the laminarization occurs for lower Ra_m numbers. In order to further illustrate this point, Fig. 6 finally shows the average Nusselt number plotted against Ra_f. The figure

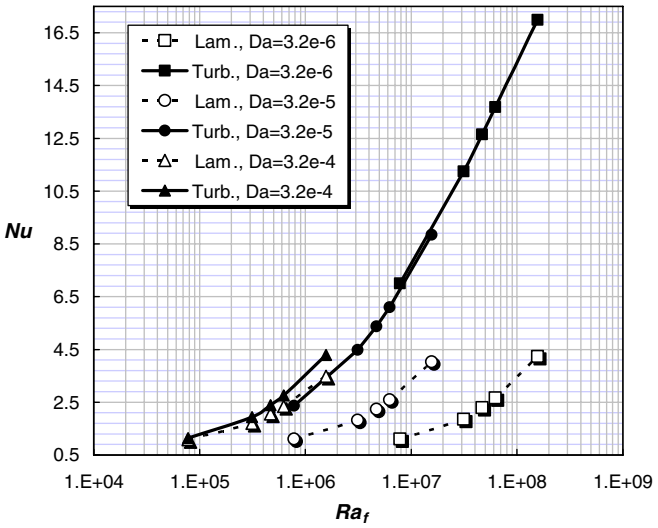

Fig. 6. Nusselt number versus fluid Rayleigh number in Table 3, $R = 2$, $k_s/k_f = 1$, $\phi = 0.8$, $Pr = 7$, $\mathbf{K}_{disp} = 0$.

seems to suggest that for lower Da, laminar and turbulence models depart from each other at an earlier value of Ra_f, corresponding then to the observed early *laminarization* phenomena mentioned above.

6. Conclusion

This work presents numerical computations for laminar and turbulent natural convection within a horizontal cylindrical annulus filled with a fluid saturated porous medium. The present simulation yielded good agreements with numerical results from Caltagirone [14]. Comparisons with experimental data, also by Caltagirone [14], show that for up to $Ra_m = 100$ calculations are within the data envelop.

Present results show that keeping with the parameters ϕ, Pr and k_s/k_f, constants, the lower the Darcy number, the

higher the difference of the average Nusselt numbers given by the two models considered. Present results show also that a lower permeability implies in an earlier *laminarization*, *i.e.*, the laminarization occurs for lower Ra_m numbers. This is probably associated with the high levels of turbulent kinetic energy in the region located at the symmetry line above the inner cylinder, inducing a higher overall heat flux from the inner surface towards the outer cylinder. In summary, a critical Rayleigh number is not clear from the results herein.

In addition to the observations above, one should mention that as more experimental data are gathered, the model herein can undergo an in deep validation for more realistic and accurate simulations. In the end, analyses of important environmental and engineering flows can benefit from the derivations herein and, ultimately, it is expected that additional research on this new subject be stimulated by the work here presented.

Acknowledgements

The authors would like to express their gratitude to the funding agencies CNPq and FAPESP, Brazil, for their invaluable support during the course of this research.

References

[1] W. Beckman, Die Warmeubertragung in Zylindrischen Gasschichten bei Naturlicher Konvektion, Forsch. Geb. Ing. Wes. 2 (1931) 165–178.
[2] H. Kraussold, Warmeabgade Von Zylindrischen Flussigkeitsschichten bei Naturlicher Konvektion, Forsch. Geb. Ing. Wes. 5 (1934) 186–191.
[3] T.H. Kuehn, R.J. Goldstein, An experimental study of natural convection heat transfer in concentric and eccentric horizontal cylindrical annuli, J. Heat Transfer 100 (1978) 635–640.
[4] M.C. Charrier-Mojtabi, A. Mojtabi, J.P. Caltagirone, Numerical solution of flow due to natural convection in horizontal cylindrical annulus, J. Heat Transfer 101 (1979) 171–173.
[5] L.S. Yao, Analysis of heat transfer in slightly eccentric annuli, J. Heat Transfer 102 (1980) 270–284.
[6] C.H. Cho, K.S. Chang, K.H. Park, Numerical simulation of natural convection in concentric and eccentric horizontal cylindrical annuli, J. Heat Transfer 104 (1982) 624–630.
[7] B. Farouk, S.I. Guceri, Laminar and turbulent natural convection in the annulus between concentric cylinders, in Symposium Volume on Natural Convection, 20th National Heat Transfer Conference, Milwaukee, Wis., 1981, pp. 143–150.
[8] A.E. McLeod, E.H. Bishop, Turbulent natural convection of gases in horizontal cylindrical annuli at cryogenic temperatures, Int. J. Heat Mass Transfer 32 (1989) 1967–1978.
[9] K. Fukuda, M. Yasutomi, S. Hasegawa, Analytical and experimental study on turbulent natural convection in a horizontal annulus, Int. J. Heat Mass Transfer 33 (1990) 629–639.
[10] Y. Miki, K. Fukuda, N. Taniguchi, Large-eddy simulation of turbulent natural convection in concentric horizontal annuli, Int. J. Heat Fluid Flow 14 (1993) 210–216.
[11] S. Kenjeres, K. Hanjalic, Prediction of turbulent thermal convection in concentric and eccentric horizontal annuli, Int. J. Heat Fluid Flow 16 (1995) 429–439.
[12] M.J.S. de Lemos, A. Sesonske, Turbulence modeling in combined convection in liquid-metal pipe flow, Int. J. Heat Mass Transfer 28 (6) (1985) 1067–1088.
[13] M.J.S. de Lemos, Anisotropic turbulent transport modeling for rod-bundle, Int. J. Heat Technol. 6 (1–2) (1988) 27–37.
[14] J.P. Caltagirone, Thermoconvective instabilities in a porous medium bounded by two concentric horizontal cylinders, J. Fluid Mech. 76 (part 2) (1976) 337–362.
[15] P.J. Burns, C.L. Tien, Natural convection in porous medium bounded by concentric spheres and horizontal cylinders, Int. J. Heat Mass Transfer 22 (1979) 929–939.
[16] A. Mojtabi, D. Quazar, M.C. Charrier-Mojtabi, An efficient finite element code for 2d steady state in a porous annulus, in: Proceedings of the International Conference of Numerical Methods for Thermal Problems, Montreal, vol. 5, 1987, pp. 644–654.
[17] M.C. Charrier-Mojtabi, J.P. Caltagirone, Numerical simulation of natural convection in an annular porous layer by spectral method, in: Proceedings of the First International Conference of Numerical Methods for Non-Linear Problems, Swannsea, 1980, pp. 821–828.
[18] M.C. Charrier-Mojtabi, Numerical simulation of two- and three-dimensional free convection flows in a horizontal porous annulus using a pressure and temperature formulation, Int J. Heat Mass Transfer 40 (7) (1997) 1521–1533.
[19] Y.F. Rao, K. Fukuda, S. Hasegawa, Steady and transient analysis of natural convection in a horizontal porous annulus with galerkin method, J. Heat Transfer 109 (1987) 919–927.
[20] K. Himasekhar, H.H. Bau, Two dimensional bifurcation phenomena in thermal convection in horizontal concentric annuli containing saturated porous media, J. Fluid Mech. 187 (1988) 267–300.
[21] M.C. Charrier-Mojtabi, A. Mojtabi, M. Azaiez, G. Labrosse, Numerical and experimental study of multicellular free convection flows in an annular porous layer, Int. J. Heat Mass Transfer 34 (1991) 3061–3074.
[22] M. Cloupeau, S. Klarsfeld, Visualization of thermal fields in saturated porous media by Christiansen effect, Appl. Optics 12 (1973) 198–204.
[23] C.T. Hsu, P. Cheng, Thermal dispersion in a porous medium, Int. J. Heat Mass Transfer 33 (1990) 1587–1597.
[24] J. Bear, Dynamics of Fluids in Porous Media, American Elsevier Pub. Co., New York, 1972.
[25] S. Whitaker, Equations of motion in porous media, Chem. Eng. Sci. 21 (1966) 291–300.
[26] S. Whitaker, Diffusion and dispersion in porous media, J. Am. Inst. Chem. Eng. 13 (3) (1967) 420–427.
[27] T. Masuoka, Y. Takatsu, Turbulence model for flow through porous media, Int. J. Heat Mass Transfer 39 (13) (1996) 2803–2809.
[28] F. Kuwahara, A. Nakayama, H. Koyama, A numerical study of thermal dispersion in porous media, J. Heat Transfer 118 (1996) 756–761.
[29] F. Kuwahara, A. Nakayama, Numerical modeling of non-Darcy convective flow in a porous medium, Heat Transfer 1998, in: Proceedings of the 11th International Heat Transfer Conference, Kyongyu Korea, vol. 4, Taylor & Francis, Washington, DC, 1998, pp. 411–416.
[30] A. Nakayama, F. Kuwahara, A macroscopic turbulence model for flow in a porous medium, J. Fluids Eng. 121 (1999) 427–433.
[31] K. Lee, J.R. Howell, Forced convective and radiative transfer within a highly porous layer exposed to a turbulent external flow field, in: Proceedings of the 1987 ASME–JSME Thermal Engineering Joint Conference, Honolulu, Hawaii, vol. 2, ASME, New, York, NY, 1987, pp. 377–386.
[32] B.V. Antohe, J.L. Lage, A general two-equation macroscopic turbulence model for incompressible flow in porous media, Int. J. Heat Mass Transfer 40 (13) (1997) 3013–3024.
[33] D. Getachewa, W.J. Minkowycz, J.L. Lage, A modified form of the k–ε model for turbulent flow of an incompressible fluid in porous media, Int. J. Heat Mass Transfer 43 (2000) 2909–2915.
[34] M.H.J. Pedras, M.J.S. de Lemos, On the definition of turbulent kinetic energy for flow in porous media, Int. Commun. Heat Mass Transfer 27 (2) (2000) 211–220.
[35] M.H.J. Pedras, M.J.S. de Lemos, Macroscopic turbulence modeling for incompressible flow through undeformable porous media, Int. J. Heat Mass Transfer 44 (6) (2001) 1081–1093.

[36] M.H.J. Pedras, M.J.S. de Lemos, Simulation of turbulent flow in porous media using a spatially periodic array and a low-*Re* two-equation closure, Numer. Heat Transfer A–Appl. 39 (1) (2001) 35–59.
[37] M.H.J. Pedras, M.J.S. de Lemos, On the Mathematical Description and Simulation of Turbulent Flow in a Porous Medium Formed by an Array of Elliptic Rods, J. Fluids Eng. 123 (4) (2001) 941–947.
[38] M.H.J. Pedras, M.J.S. de Lemos, Computation of turbulent flow in porous media using a low Reynolds k–ε model and an infinite array of transversally-displaced elliptic rods, Numer. Heat Transfer A – Appl. 43 (6) (2003) 585–602.
[39] F.D. Rocamora Jr., M.J.S. de Lemos, Analysis of convective heat transfer of turbulent flow in saturated porous media, Int. Commun. Heat Mass Transfer 27 (6) (2000) 825–834.
[40] M.J.S. de Lemos, F.D. Rocamora, Turbulent transport modeling for heated flow in rigid porous media, in: Proceedings of the Twelfth International Heat Transfer Conference, 2002, pp. 791–795.
[41] M.J.S. de Lemos, E.J. Braga, Modeling of turbulent natural convection in saturated rigid porous media, Int. Comm. Heat Mass Transfer 30 (5) (2003) 615–624.
[42] E.J. Braga, M.J.S. de Lemos, Turbulent natural convection in a porous square cavity computed with a macroscopic k–ε model, Int. J. Heat Mass Transfer 47 (26) (2004) 5635–5646.
[43] E.J. Braga, M.J.S. de Lemos, Heat transfer in enclosures having a fixed amount of solid material simulated with heterogeneous and homogeneous models, Int. J. Heat Mass Transfer 48 (23–24) (2005) 4748–4765.
[44] E.J. Braga, M.J.S. de Lemos, Laminar natural convection in cavities filled with circular and square rods, Int. Commun. Heat Mass Transfer 32 (10) (2005) 1289–1297.
[45] M.J.S. de Lemos, M.S. Mesquita, Turbulent mass transport in saturated rigid porous media, Int. Comm. Heat Mass Transfer 30 (1) (2003) 105–113.
[46] M. Saito, M.J.S. de Lemos, Interfacial heat transfer coefficient for non-equilibrium convective transport in porous media, Int. Commun. Heat Mass Transfer 32 (5) (2005) 667–677.
[47] M. Saito, M.J.S. de Lemos, A correlation for interfacial heat transfer coefficient for turbulent flow over an array of square rods, J. Heat Transfer 128 (2006) 444–452.
[48] M.J.S. de Lemos, L.A. Tofaneli, Modeling of double-diffusive turbulent natural convection in porous media, Int. J. Heat Mass Transfer 47 (19–20) (2004) 4233–4241.
[49] R.A. Silva, M.J.S. de Lemos, Numerical analysis of the stress jump interface condition for laminar flow over a porous layer, Numer. Heat Transfer Part A – Appl. USA 43 (6) (2003) 603–617.
[50] R.A. Silva, M.J.S. de Lemos, Turbulent flow in a channel occupied by a porous layer considering the stress jump at the interface, Int. J. Heat Mass Transfer USA 46 (26) (2003) 5113–5121.
[51] M.J.S. de Lemos, Turbulent kinetic energy distribution across the interface between a porous medium and a clear region, Int. Commun. Heat Mass Transfer 32 (1–2) (2005) 107–115.
[52] M.J.S. de Lemos, R.A. Silva, Turbulent flow over a layer of a highly permeable medium simulated with a diffusion-jump model for the interface, Int. J. Heat Mass Transfer 49 (3–4) (2006) 546–556.
[53] M.J.S. de Lemos, M.H.J. Pedras, Recent mathematical models for turbulent flow for saturated rigid porous media, J. Fluids Eng. 123 (4) (2001) 935–940.
[54] M. Assato, M.H.J. Pedras, M.J.S. de Lemos, Numerical solution of turbulent channel flow past a backward-facing step with a porous insert using linear and nonlinear k–ε models, J. Porous Media 8 (1) (2005) 13–29.
[55] N.B. Santos, M.J.S. de Lemos, Flow and heat transfer in a parallel plate channel with porous and solid baffles, Numer. Heat Transfer A 49 (5) (2006) 471–494.
[56] S. Ergun, Fluid flow through packed columns, Chem. Eng. Proc. 48 (1952) 89–94.
[57] A. Nakayama, F. Kuwahara, A macroscopic turbulence model for flow in a porous medium, J. Fluids Eng. 121 (1999) 427–433.
[58] B.E. Launder, D.B. Spalding, The numerical computation of turbulent flows, Comput. Methods Appl. Mech. Eng. 3 (1974) 269–289.
[59] S.N. Lane, R.J. Hardy, Porous Rivers: a new way of conceptualizing and modeling river and floodplain flows? in: D. Ingham, I. Pop (Eds.), Transport Phenomena in Porous Media II, first ed., Pergamon Press, 2002, pp. 425–449 (Chapter 16).
[60] S.V. Patankar, D.B. Spalding, A calculation procedure for heat, mass and momentum transfer in three dimensional parabolic flows, Int. J. Heat Mass Transfer 15 (1972) 1787–1806.
[61] H.L. Stone, Iterative solution of implicit approximations of multi-dimensional partial differential equations, SIAM J. Numer. Anal. 5 (1968) 530–558.
[62] A.A. Merrikh, A.A. Mohamad, Non-Darcy effects in buoyancy driven flows in enclosures filled with vertically layered porous media, Int. J. Heat Mass Transfer 45 (2002) 4305–4313.